Dry calibration of electromagnetic flowmeters based on numerical models combining multiple physical phenomena (multiphysics)

X. Fu,[1] L. Hu,[1,a)] K. M. Lee,[2] J. Zou,[1] X. D. Ruan,[1] and H. Y. Yang[1]
[1]*State Key Laboratory of Fluid Power Transmission and Control, Zhejiang University, Hangzhou 310027, China*
[2]*Woodruff School of Mechanical Engineering, Georgia Institute of Technology, Atlanta, Georgia 30332-0405 USA*

(Received 3 March 2010; accepted 10 September 2010; published online 26 October 2010)

This paper presents a method for dry calibration of an electromagnetic flowmeter (EMF). This method, which determines the voltage induced in the EMF as conductive liquid flows through a magnetic field, numerically solves a coupled set of multiphysical equations with measured boundary conditions for the magnetic, electric, and flow fields in the measuring pipe of the flowmeter. Specifically, this paper details the formulation of dry calibration and an efficient algorithm (that adaptively minimizes the number of measurements and requires only the normal component of the magnetic flux density as boundary conditions on the pipe surface to reconstruct the magnetic field involved) for computing the sensitivity of EMF. Along with an in-depth discussion on factors that could significantly affect the final precision of a dry calibrated EMF, the effects of flow disturbance on measuring errors have been experimentally studied by installing a baffle at the inflow port of the EMF. Results of the dry calibration on an actual EMF were compared against flow-rig calibration; excellent agreements (within 0.3%) between dry calibration and flow-rig tests verify the multiphysical computation of the fields and the robustness of the method. As requiring no actual flow, the dry calibration is particularly useful for calibrating large-diameter EMFs where conventional flow-rig methods are often costly and difficult to implement. © *2010 American Institute of Physics*. [doi:10.1063/1.3499643]

I. INTRODUCTION

In the last few decades, electromagnetic methods for measuring water flow rate have become more and more widespread owning to its high precision, no pressure loss, nonpolluting and high reliability. These advantages are attributed to Faraday's law of electromagnetic induction; a potential difference is induced between a pair of appropriately located electrodes as conductive liquid flows through the magnetic field in a measuring pipe. The flow rate can be accurately determined from the measured magnitude of the induced voltage signal.[1]

To ensure product reliability and accurately account for water, electromagnetic flowmeters (EMFs) must be accurately calibrated (before leaving factory or used for a period of time).[2] At present, most flowmeters are calibrated using flow-rigs as illustrated by Fig. 1 where the calibrated EMF is installed between two long straight pipes. In Fig. 1, water flowing at steady state is supplied by a high-power pump along with an underground water reservoir and a tall water tower (or buffer tank) that serves as a constant water-level (and hence pressure head) buffer tank. The flow rig calibration setup determines the precision of the EMF by comparing the total water volume measured by the EMF for a specified period of time against the actual volume accumulated in the standard metal tanks. While straight forward, conventional flow-rigs have two obvious shortcomings when used to calibrate large EMFs (with diameter in the order of 1 m). First, flow-rig calibration of large EMFs is costly and time consuming. It was estimated that using a flow-rig to calibrate a 1.2 m-diameter EMF would require a 250 kW pump to supply water flow of 1.5 t/s, and the process would take 2–4 h at a cost about 3 000 000 pounds.[3] Second, a minimum of ten pipe diameters of straight run upstream and five diameters downstream is recommended for a typical flow-rig setup.[2] This specification to ensure that the flow passing through the EMF is fully developed, however, often cannot be met (especially for large EMFs) resulting in additional errors in many actual applications where space to house the required long pipes is limited.

In contrast, "dry calibration" requires no actual liquid flow and can predict the EMF performances for special flow structures; thus, it is considered as an effective alternative of the flow-rig method, especially for large EMFs. As early as in 1980s, Bevir *et al.*[4,5] introduced a dry-calibration method based on scanning the alternating magnetic field (240 Hz) on

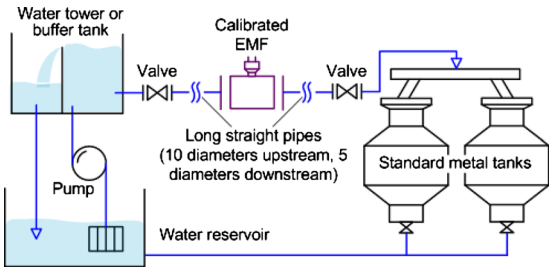

FIG. 1. (Color online) Illustration of the flow-rig calibration.

a)Electronic mail: cmeehuli@zju.edu.cn.

the surface of an insulating flow tube with a search coil followed by analytical computations to predict sensitivity.[5] This earlier dry-calibration method, which focused on medical research[4–7] and primarily for small-diameter (20 mm) blood flow EMFs, has a 3% calibration error (compared against experimental data). Although the calibration errors are too large for water-flow rate-measuring EMFs, the theoretical basis of dry calibration remains valuable in the follow up studies by many others; for examples, Baker and Hemp presented their methods for dry calibration of EMFs based on this theory.[8,9]

Increase in water supply and transmission systems has motivated researchers to develop dry-calibration technology for calibrating large EMFs. Among these, POTOK (developed by Velt and Mikhailova), which uses a magnetic field converter (MFC) in the form of an induction coil constructed in accordance with the surface weighting function, enables one to simulate instruments of different construction and for different hydrodynamic regimes and flow structures.[10,11] The device is applicable for dry calibrating EMFs with channel diameters from small values (order of several millimeters) to indefinitely large values (up to 2000 mm or more).[11] However, POTOK requires additional comparison tests (between dry calibration and flow-rig calibration) to obtain a correct factor for each MFC. Typically, POTOK has a calibration error after correction of about 0.5% as compared against experimental data on a flow-rig setup. In addition to this drawback, the induction coil in the MFC must be specially designed and manufactured for each flow structure.[12] Another low-cost technique (proposed by Hemp[3,13] for calibrating large EMFs) fills the flowmeter tube with water and measures the axial component of the eddy current electric field in the water over each electrode. Hemp's technique, which experimentally simulates a normal flowmeter operation, allows the calibration factor for a flat velocity profile to be determined.

This paper presents a dry-calibration method based on numerical computation of multiphysics, which has become an important approach[14–16] to solve applied physical problems as computer technologies continue to advance. As will be introduced, this calibration method is highly precise (with less than 0.3% error as compared against tests on flow-rigs) for medium and large EMFs (from 200 mm in diameter) without the need of additional correction, and can be used to predict the performance of an EMF for special flow structures. The remainder of this paper offers the followings:

- The governing partial differential equations (PDEs) that characterize multiphysical coupling phenomenon in flow measurements based on Faraday's law of electromagnetic induction are formulated. The PDEs, along with a complete set of boundary conditions (BCs), provide a basis to solve for the coupling magnetic, flow and electric fields in the EMF, upon which a basic formula is derived to calculate the induced voltage in terms of the structural sizes of the flowmeter.
- In the context of an EMF, measurement methods to determine the distribution of the normal flux density B_r on the pipe surface as BCs and the measuring volume (MV) for solving the PDEs are introduced. The method based on an adaptive algorithm minimizes the number of measurements without sacrificing the accuracy of specified magnetic BC. The method to determine the pipe diameter based on the B_r morphology and the specified geometry (size and position) of the electrodes is also introduced.
- A numerical model for solving the governing PDEs with measured BCs, which characterize the coupling multiphysics of an EMF, is built for computing the EMF sensitivity. Two important considerations to ensure the calibration precision are also discussed; estimation of the magnetic field in the measurement-dead-domain (MDD), and structured grid based on equal-area transformation of the electrodes.
- Two experimental verifications of dry calibration using automated BC measurements have been made on an actual EMF by comparing results against flow-rig calibration. As will be demonstrated, the relative difference in the sensitivity between dry-calibration and flow-rig test methods is less than 0.3% for fully developed flow (with sufficiently long straight pipes at both the upstream and the downstream). The effect of flow disturbance on the flowmeter measuring error (relative to flow-rig calibration) has been experimentally studied by installing a baffle at the inflow port of the EMF. Good agreements of the error curves corresponding to different baffle heights and different flow rates further well verify the multiphysical models.

II. MULTIPHYSICAL ANALYSIS AND BASIC EQUATIONS

When relativistic terms are negligible, the Ohm's law that relates the electric field to fluid flow leads to Eq. (1) in Shercliffs study[1]

$$\mathbf{j} = \sigma(\mathbf{E} + \mathbf{v} \times \mathbf{B}), \tag{1}$$

where $\mathbf{j}$ is the current density vector; σ is the fluid conductivity; $\mathbf{E}$ is the electric filed in the stationary coordinate system; $\mathbf{v}$ is the fluid velocity; and $\mathbf{B}$ is the magnetic flux density. In Eq. (1), $(\mathbf{E}+\mathbf{v}\times\mathbf{B})$ is the electric field relative to the moving fluid, in which the term $\mathbf{v}\times\mathbf{B}$ represents the electromotive force induced by the fluid motion; and $\mathbf{E}$ accounts for the charges distributed in and around the fluid and due to any variation in the magnetic field in time.[1] In a fluid of uniform conductivity ($\nabla\sigma=0$), it has been verified that[2]

$$\nabla^2 U = \nabla \cdot (\mathbf{v} \times \mathbf{B}), \tag{2}$$

where U is the electrical potential and $E=-\nabla U$. Equation (2) and an appropriate set of BCs are the basis for solving the U distribution of an EMF for given $\mathbf{v}$ and $\mathbf{B}$ distributions.

From Eq. (2) with the two BCs, $v=0$ and $\partial U/\partial r=0$, at the insulating pipe wall of an EMF,[1,22] the integral equations to calculate the output potential difference ΔU_{EE} between its electrodes have been derived[4,17] with the help of a Green's function

$$\Delta U_{EE} = \int_{\Omega} (\mathbf{v} \times \mathbf{B}) \cdot \mathbf{j}_{\mathbf{v}} d\Omega, \tag{3a}$$

$$\text{or} \quad \Delta U_{EE} = \int_{\Omega} (\mathbf{v} \times \mathbf{B}) \cdot \mathbf{W} d\Omega, \tag{3b}$$

where Ω denotes the MV. The virtual current $\mathbf{j}_{\mathbf{v}}$ of Eq. (3a) and the weight function $\mathbf{W}$ of Eq. (3b), which are defined in Refs. 4 and 17, respectively, have same distributions and physical meanings (expressing how the induced voltages contribute to the output signal at the electrodes from different positions in the MV). In this paper, the weight function $\mathbf{W}$ is selected as a common symbol for generality; thus, Eq. (3b) is used to calculate the induced signal ΔU_{EE}. For this, the field ($\mathbf{W}$, $\mathbf{B}$, and $\mathbf{v}$) distributions in the MV can be learned from the solutions to the special field governing PDEs given below.

A. Governing PDE of W

When deriving Eq. (3a) from Eq. (2) with a Green's function G, an additional vector function $\mathbf{W}$ is introduced. In physics, this function is determined by the measuring pipe geometries (including the pipe size, and the size and positions of the electrodes). Mathematically, $\mathbf{W}$ is the gradient of the scalar function G and solution to Laplace's equation subject to the BCs determined by those boundary geometries; and can be calculated according to following equations:[5,17,22]

$$\mathbf{W} = \nabla G, \tag{4a}$$

$$\nabla^2 G = 0, \tag{4b}$$

$$\left.\frac{\partial G}{\partial n}\right|_{\Gamma} = \begin{cases} \pm 1/S_{\mathrm{E}} & \text{electrodes}, \\ 0 & \text{other}. \end{cases} \tag{4c}$$

In Eq. (4c), Γ is the MV boundary surface and S_{E} is a small area on the electrode end surface. The value of the BCs is positive on one electrode surface, and negative on the other.

B. Governing PDE of B

The $\mathbf{B}$ vector field distribution in the MV can be solved from Eq. (5), in which current corresponding to the conductive fluid motion is ignored, and $\mathbf{B}$ is expressed in terms of a magnetic scalar potential ψ defined in Eq. (5a):

$$\mathbf{B} = -\mu \nabla \Psi, \tag{5a}$$

$$\nabla^2 \Psi = 0, \tag{5b}$$

$$\begin{cases} \Psi|_{\Gamma_1} = \Psi_0, \\ \left.\dfrac{\partial \Psi}{\partial n}\right|_{\Gamma_2} = -\dfrac{B_n}{\mu}, \end{cases} \tag{5c}$$

where μ is the magnetic permeability of the fluid in the MV; Γ_1 and Γ_2 denote special boundary portions, on which Dirichlet BC (DBC) and Neumann boundary condition (NBC) are specified, respectively, to solve the Laplace's equation [Eq. (5b)] for ψ. In detail, the first equation of Eq. (5c) specifies a given function Ψ_0 as DBC on the boundary portion Γ_1 and the second equation gives NBC (or the normal derivative of Ψ) on Γ_2. In the equation, B_n specifies the distribution of normal flux density on this boundary portion.

As discussed in our previous paper,[18] the potential Ψ is not measurable in practice. With few exceptions (such as magnetically ground surface or remote far field where Ψ can be reasonably approximated and arbitrarily set to zero[18]), knowing its distribution on the boundary surface is nearly impossible. As will be discussed, magnetic sensors (such as a Hall sensor) are available to measure the B_n distribution, and thus measured NBC are commonly used in practice to help specify the complete set of BCs required for solving the Laplace's equation [Eq. (5b)].

C. Governing PDE of v

The velocity profile $\mathbf{v}$ of the fluid flowing through the EMF can be solved from the incompressible Navier–Stokes (NS) equations given in Eq. (6a) (consisting of the momentum transport equation and the continuity equation for incompressible fluids) along with BCs specified in [Eq. (6b)]:[19]

$$\begin{cases} \rho \dfrac{\partial \vec{V}}{\partial t} - \nabla \cdot [\eta(\nabla \vec{v} + (\nabla \vec{v})^{\mathrm{T}})] + \rho(\vec{v} \cdot \nabla)\vec{v} + \nabla p = \vec{F}, \\ \nabla \cdot \vec{v} = 0, \end{cases} \tag{6a}$$

$$\begin{cases} [-p\vec{I} + \eta(\nabla \vec{v} + (\nabla \vec{v})^{\mathrm{T}})]\vec{n}|_{\Gamma_1} = -p_0 \vec{n}, \\ \vec{v}|\Gamma_2 = \vec{v}_0, \end{cases} \tag{6b}$$

where p is the pressure; ρ is the density; η is the dynamic viscosity; and $\vec{F}$ is a volume force field such as gravity. The solution domain of Eq. (6b) depends on actual flow pipe. Equation (6b) gives two commonly used BCs specifying pressure distribution p_0 and velocity distribution $\vec{v}_0$ on the boundary, respectively. In practice, the flow fields in the upstream and downstream pipes are commonly included with that in the EMF in the calculation, and generally, the normal velocity distribution at the inflow port and the constant pressure at the outflow port are measured. In addition, nonslip wall BCs ($\vec{v}_0 = 0$) are specified on the pipe walls.

To complete the formulation, the BCs and MV are measured so that these PDEs can be solved for calculating the sensitivity according to Eq. (3b). This is discussed in Secs. III A and III B.

III. MEASUREMENTS TO SPECIFY BCS AND MV

The required BCs for calculating $\mathbf{v}$ [Eq. (6b)] can be determined according to actual flow conditions. The other BCs for $\mathbf{W}$ in Eq. (4c) and $\mathbf{B}$ in Eq. (5c) can be calculated through special measurements on the calibrated EMF. The geometrical size Ω, of the MV in Eq. (3b) can be determined through measurements. Thus, two kinds of measurements are required on the flowmeter; magnetic measurement to determine B_n in Eq. (5c); and geometrical measurement to determine BCs for calculating $\mathbf{W}$ [Eq. (4c)] and the MV Ω, in Eq. (3b).

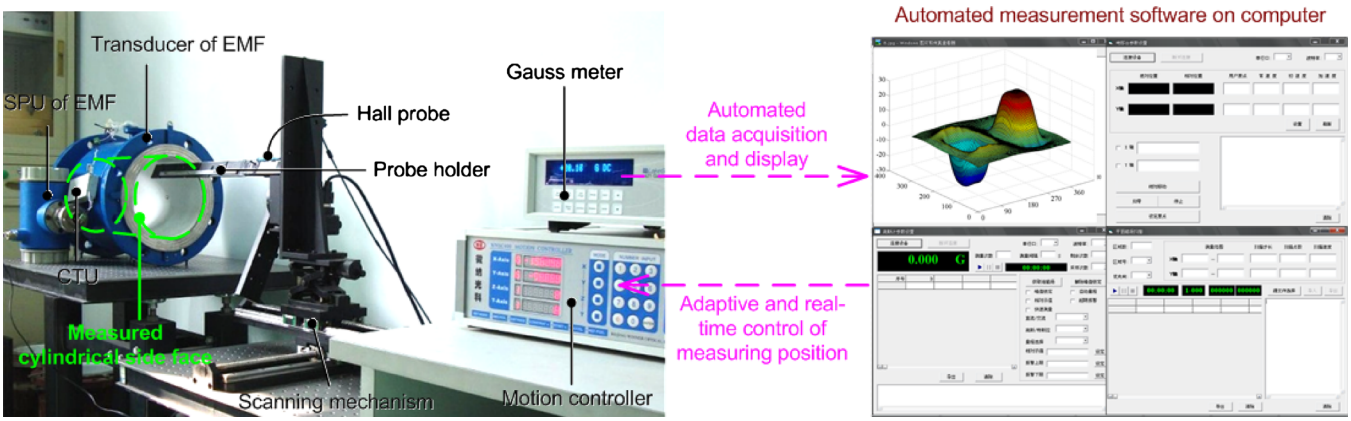

FIG. 2. (Color online) Automated measurement setup of normal flux density B_n (adapted from Ref. 18).

A. Measurement of normal flux density B_n

1. Measurement setup

As introduced in Ref. 18, the normal magnetic flux density on the boundary surface is measured with a Hall probe on the aluminum holder positioned by a computer controlled scanning servo mechanism as shown in Fig. 2 so that highly accurate data acquisition (with maximum error within $\pm 0.20\%$) can be automated:[18]

- Located near the end of the probe (monitored by the gauss meter), the diameter of Hall-effect area (in the MV invisible in the figure), where the average value of the normal **B** component passing through this small area, is about 1 mm. Pulsed dc currents that excite the alternating magnetic field are used by most existing EMFs to avoid polarization effects on the electrodes. However, it is much more difficult to accurately measure such alternating magnetic field than a static magnetic field. As for the Hall probe in our setup (Fig. 2), the error in measuring an ac field is about ten times that in a static field. Thus, a current transformation unit (CTU), inside which is a full-wave rectifier circuit based on a four-diodes bridge,[20] is connected between the signal processing unit (SPU) and the transducer of the EMF. The CTU transforms the pulsed-dc exciting current to a constant-dc current, and accordingly builds an easily-measurable static magnetic field in the MV. The static field has same strength and distribution with the alternating field, and will not cause polarizations on electrodes because no water filled in the pipe during dry calibration.
- The gauss meter, the algorithm that monitors the autoscanning procedure and the position servomechanisms are controlled by a host computer. The rotational and translational resolutions of magnetic scanning device are 0.005° and 5 μm, respectively.

2. Adaptive scanning algorithm

A practical challenge is to minimize the number of measurements without sacrificing the accuracy of specified B_n. It is also desired that the method can be applied to different type EMFs without prior knowledge of the B_n morphology when selecting measured points in real-time. For this, an adaptive scanning algorithm is written to curve-fit four nearest calibrated points (B_{n-3}, B_{n-2}, B_{n-1}, and B_n) as a basis to select the location guided by a chord-height and data-spacing (CH&DS) criterion to take the next measurement B_{n+1} as illustrated in Fig. 3(a). In Fig. 3(a), h is the perpendicular distance from B_n to the search line from B_{n-1}, l_1, and l_2 are the straight-line distances between B_{n-1} and B_n, and between B_n and the searched point B' on the B_n-tangent line. The next measurement point B_{n+1} is extrapolated from B_n along its tangent as follows. This begins with a search line (originated from the previous measurement B_{n-1}) to intercept the B_n-tangent line at B' such that a chord-height h can be defined quantitatively. To avoid undesirably low density

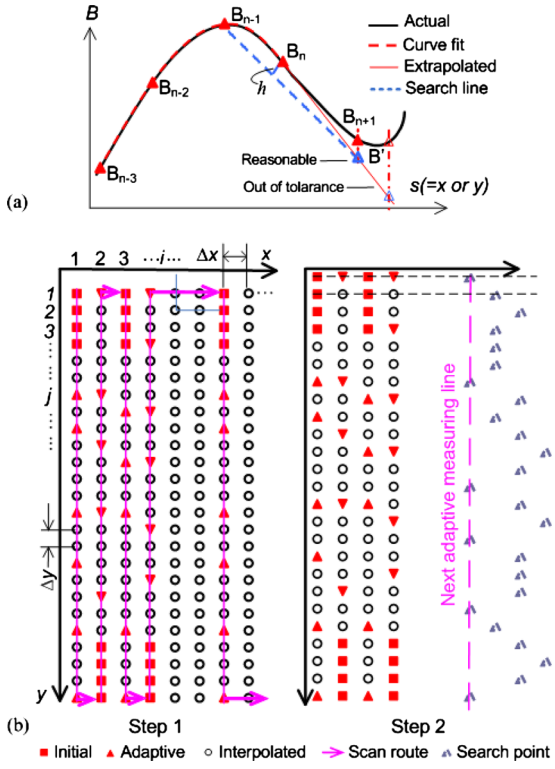

FIG. 3. (Color online) Adaptive scanning algorithm based on CH&DS criterion: (a) schematics illustrating chord-height criterion; (b) illustration of the adaptive measuring process: step 1. Scan along y with constant incremental x; step 2, scan along x with incremental y.

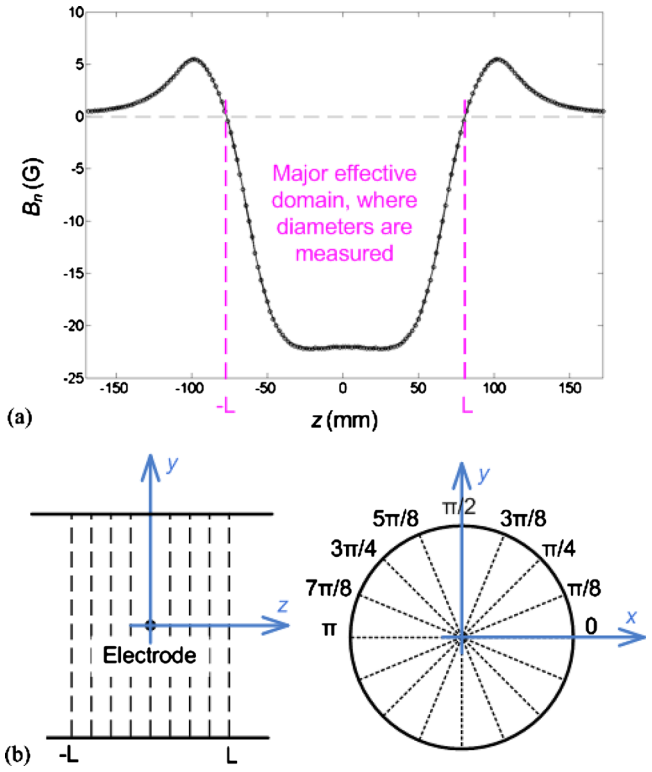

FIG. 4. (Color online) Selecting diameter measured positions based on B_n morphology: (a) Measured B_n morphology along z-direction (θ=n/2); (b) Illustration of diameter measured positions.

samples around a local maximum or minima [as illustrated in Fig. 3(a)], the data-spacing l_2 is introduced as a design parameter. Thus, the selection of measuring points (MPs) involves two independent thresholds: chord-height threshold CH and data spacing threshold DS. A common technique to locate the point for taking the next measurement is to rotate the search line about (s_{n-1}, B_{n-1}) incrementally until $h \approx$CH or $l_2 \approx$DS. Figure 3(b) provides an overview of the scanning algorithm which scans along increasing y then decreasing y in a specified incremental x:

Step 1 (scan along y with constant incremental x). The scan begins (at $i=1$) with four initial (equally spaced Δy) measurements to provide a cubic spline curve-fit. The next MP is then determined using the selection criteria (CH, DS); the actual value B_{n+1} is measured at y_{n+1}. Finally, the values of the unmeasured (equally spaced) nodes are then interpolated from the measured points. Using the four latest nodes, step 1 is repeated until all nodes in regions ($1 \le i \le 4$, y) are measured or interpolated.

Step 2 (scan along x with incremental y). For each constant-y row, the next MP along x is determined from the measured or interpolated nodes using the same criterion as in step 1 (with y replaced by x); Since above process could result in different i values for different j, the minimum i value (or i_{min}) is selected to begin the new scanning route; step 1 is repeated and unmeasured nodes before i_{min} column are interpolated.

Steps 1 and 2 are repeated until all the nodes on the BC surface are specified.

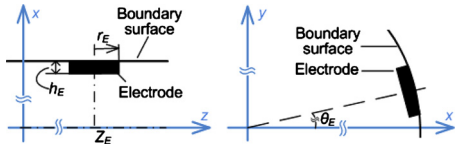

FIG. 5. (Color online) Illustration of position parameters (θ_E, Z_E) and size parameters (r_E, h_E) for electrodes.

B. Geometrical measurement of the EMF transducer

1. Measurement of MV

The cylindrical MV involves two parameters; diameter D_0 and length L_0. In practice, the actual MVs are not strictly cylindrical (especially near the ports of the EMF, where insulating linings of the pipe must be bent 90° to bond with a flange), due to which several diameters at different positions are required to calculate an average. In this study, the measured positions of the diameter are selected according to the measured B_n morphology in Sec. III A. Taking the B_n morphology in Fig. 4 as an example, it is measured on the boundary surface of an actual EMF along z-direction where $\theta=\pi/2$ ($\theta=0$ and π at the electrodes). Strong magnetic field only exists in the domain $-L \le z \le L$ ($L \approx 80$ mm for this flowmeter) corresponding to the structure size of the U-shaped EM insider the flowmeter (will be introduced in detail shortly). Accordingly, the output voltage between the electrodes is primarily contributed by the moving fluid in this major effective domain (MED) of the flowmeter, where relatively strong distribution of **W** exists. Diameters measured in the MED with uniform intervals both in z and θ directions [L/4 and $\pi/8$, respectively, in Fig. 4(b)] are averaged.

2. Measurements of the electrodes

Most actual EMF electrodes have circular end-face and inserted into the pipe with a small depth. The geometrical parameters required to specify the electrodes are illustrated in Fig. 5, where (θ_E, Z_E) and (d_E, h_E) specify the position and size of the electrode, respectively. All of them can be measured with special measuring tools such as inside-micrometer and vernier caliper, etc.

IV. MULTIPHYSICAL COMPUTATION MODEL

Figure 6 illustrates a typical multiphysical computation model used in the proposed dry calibration. The EMF (domain II) is installed between the upstream and downstream

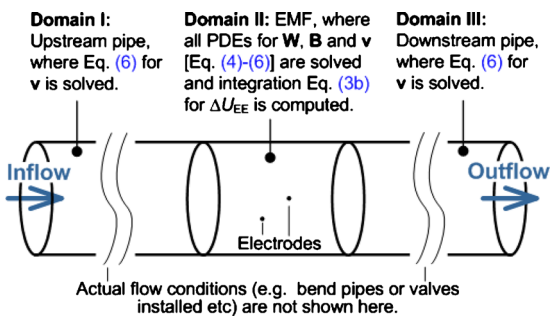

FIG. 6. (Color online) Illustration of numerical multi-physics computation model.

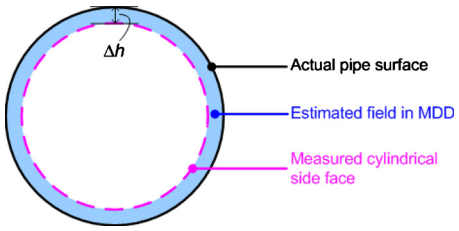

FIG. 7. (Color online) Estimation of the immeasurable field in MDD.

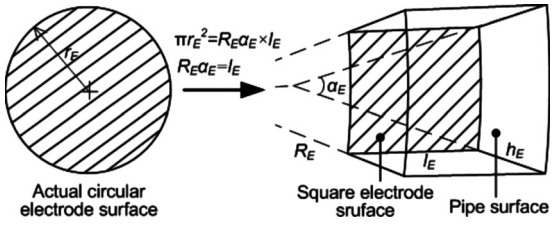

FIG. 8. Equal-area transformation of the electrodes.

pipes (domains I and III, respectively). To obtain the actual velocity field **v** of the conducive fluid passing through the calibrated EMF, the NS equations [Eq. (6)] are solved in all three domains with nonslip BCs ($v=0$ m/s) on the pipe walls and measured normal velocity distribution and the constant pressure on the inflow and outflow ports, respectively. The PDEs, Eqs. (4) and (5), are only required in domain II to solve for **W** and **B** in the EMF where the induced signal ΔU_{EE} between the electrodes is calculated from Eq. (3b). To solve for **W**, Neumann BCs, $\partial G/\partial n = \pm 1/S_E$ and $\partial G/\partial n = 0$, are specified on the electrode surfaces and on the remaining boundary surfaces, respectively. For **B**, a data link is built between the model and a file containing data of the measured normal flux density B_n at every measured position so that BC values between measured data points on the boundary surface can be interpolated.

Finite-element method is used to solve the PDEs and compute the final sensitivity integral. Two important considerations to ensure the computation precision are worthy of mentioning:

A. Estimate Field in MDD

When measuring the normal flux density B_n (Fig. 2), the scanning probe must not be too close to the pipe surface to avoid accidental collision during scanning; this commonly results in a narrow MDD gap Δh (≤ 10 mm) as illustrated in Fig. 7. To obtain the field distribution in the MDD for accurate calibration, the BC on the pipe surface is extrapolated (with linear or cubic spline methods) and then iteratively optimized from the field reconstructed by the measured BC. The field in the MDD is then reconstructed by solving the PDEs with BCs specified by the estimated BC on the pipe surface.

B. Structured grid based on equal-area transformation of the electrodes

Domain II (Fig. 6) is meshed with structured grids to ensure accurate integration (high-order, such as fourth order) of Eq. (3b). For this requirement, circular electrode surfaces are transformed to square ones to facilitate generating structured grids around them. Since Neumann BCs $\partial G/\partial n = \pm 1/S_E$ are specified on the electrodes, the transformation based on equal-area criterion (given by the equations in Fig. 8) ensures no change in calculating the weight function.

V. EXPERIMENTAL VERIFICTAION AGAINST FLOW-RIG CALIBATION

A. Tested EMF

Dozens of EMFs from three different manufacturers were tested by the authors. Among the tested flowmeters, the smallest diameter is 200 mm. Dry calibration of a small-diameter EMF is more difficult than that of a large-diameter EMF for the same percentage error in BC scanning because smaller dimension means a more stringent requirement in terms of absolute positional accuracy for a similar task. Thus, it is expected that test results based on the smallest diameter of 200 mm will give a more convincing illustration of the dry calibration.

1. Inner structure of the EMF

Figure 9 shows an EMF consisting of a measuring pipe and a magnetic unit. The latter excites an induction (between the electrodes as conductive liquid flows through the magnetic field) through a pair of U-shaped electromagnets. The actual flowmeter consists of other components (yoke, shield layer, sailing layer, and signal lead channel, etc., not shown in the figure). However, the reconstruction of the magnetic field in the cylindrical pipe (MV) and following calibration of the flowmeter does not require the knowledge of the magnetic structure.

2. Measured BCs and MV

The measured geometries of the measuring pipe and electrodes as well as the mapped dimensions of the square electrodes are listed in Table I. With these data, the MV and BCs of the weight function **W** can be determined. The diameter D_0 is an average of several measured diameters (position and values given in Table IV in Appendix); the maximum difference among the measured diameters at different positions is up to 4 mm or 2% of the average data D_0.

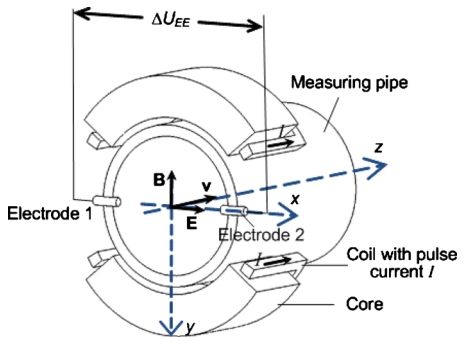

FIG. 9. (Color online) Inner structure of the tested EMF.

TABLE I. Measured geometry sizes of the EMF.

Parameters		Values
Average MV diameter and length	(D_0, L_0)	(200.273 mm, 340 mm)
Electrode positions and sizes	$(\theta_{E1}, Z_{E1}, d_{E1}, h_{E1})$	(0, 0 mm, 10.18 mm, 0.977 mm)
	$(\theta_{E2}, Z_{E2}, d_{E2}, h_{E2})$	(π, 0 mm, 10.18 mm, 0.977 mm)
Size of transformed square electrode	(R_E, α_E, L_E)	(99.16 mm, 5.213°, 9.0218 mm)

To obtain the BCs for reconstructing the magnetic field, the normal flux density B_r at $r=90.7$ mm were measured point by point under the control of the scanning setup shown in Fig. 2 with CH=0.2 G, $DS_\theta=9°$, and $DS_z=6$ mm. The CH threshold of 0.2 G corresponds to about 1% of the maximum BC value while the DS thresholds in θ and z directions are both three times of the step length required according to Shannon's sampling theorem in equal-spaced methods.[18] Benefited from the CH&DS criterion, many BC measurements at small local curvature positions are exempted resulting only 2,725 measurements needed, which were completed in about 27 min with a total scanning route length of 37.68 m. The final MPs distribution is given in Fig. 10(a), where the colored points denotes that the measured magnitude of the magnetic flux density in Fig. 10(b) and white color means no measurement.

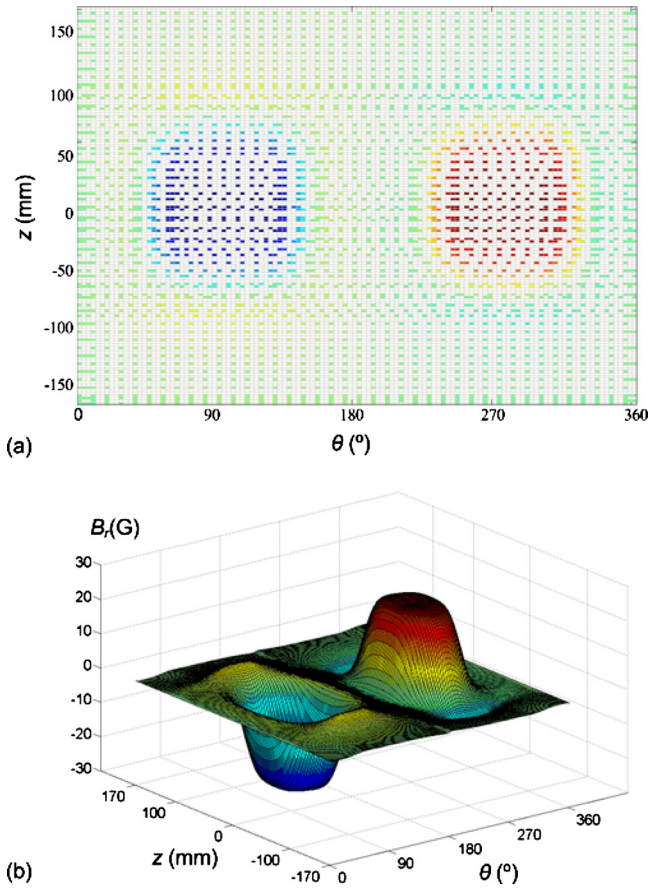

FIG. 10. (Color online) Adaptive measurement of B_r at $r=90.7$ mm: (a) MP distribution (2725 points); (b) measured B_r.

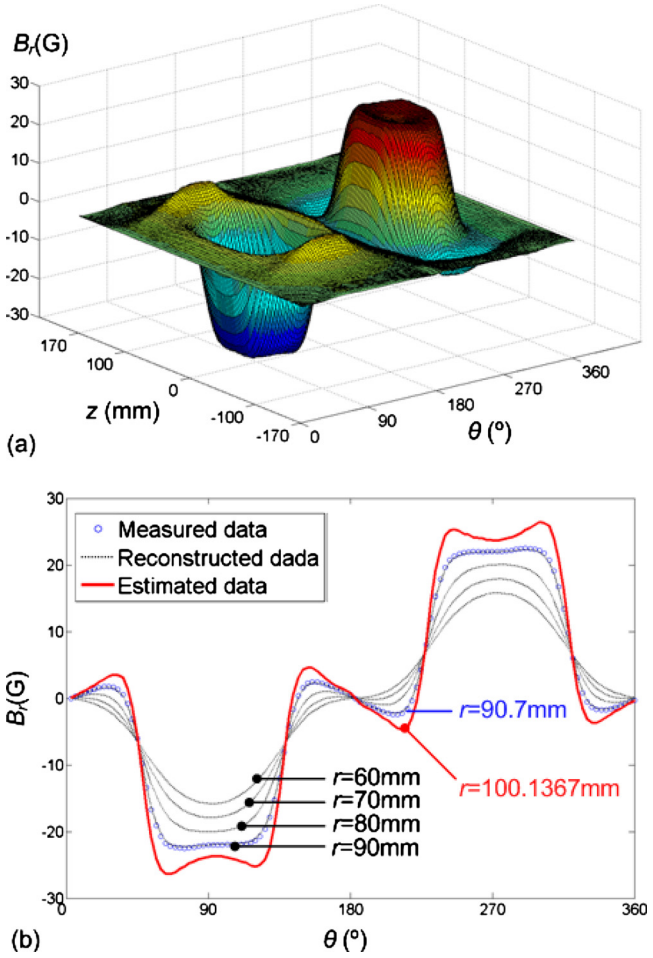

FIG. 11. (Color online) Estimation of B_r on actual pipe surface ($r=100.1367$ mm): (a) estimated B_r at $r=100.1367$ mm; (b) illustration of the extrapolation at $z=0$ mm.

The MDD has a gap of 9.4367 mm between the two surfaces; which is the difference between the radius of the scanned cylindrical side surface, 90.7 mm, and that of the actual pipe surface given in Table I, 100.1367 mm. To obtain the BC data at the actual surface, the B_r data at $r=100.1367$ mm are estimated from the reconstructed field in the domain where $r \leq 90.7$ mm. The B_r data at $r=60$, 70, 80 and 90 mm are used as bases for the extrapolation during the estimation. These surfaces are selected with equal interval of 10 mm (approximately the MDD depth of 9.4367 mm) for the extrapolation accuracy.[21] The estimated B_r at $r=100.1367$ mm is given in Fig. 11(a). The source data at $r=60$, 70, 80, and 90 mm are given in the Appendix (Figure 17). Here, the data at $z=0$ mm (where the electrodes locate) are selected to illustrate the extrapolation [Fig. 11(b)].

3. Computed distributions of W and B

The calculated **W** and **B** distributions are given in advance here to help illustrate the EMF design features using the results of dry calibration. The **W** and **B** fields in Figs. 12 and 13, which are slices at $z=0$, show that they are nearly orthogonal to each other. As shown in Fig. 12, the weight function **W** is much stronger near the electrodes as determined by the BCs in Eq. (4c). This means that the stream-

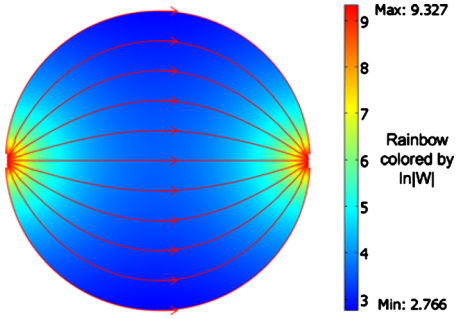

FIG. 12. (Color online) Sliced contour and streamlines of **W** at $z=0$ nm.

lines only pass through the electrode surfaces but not any other areas on the pipe surface. Figure 13 shows the computed (reconstructed) magnetic field excited by the U-shaped electromagnets (Fig. 9). The field is strong near the U-shaped core but much weaker around the electrodes. In other words, the nearly orthogonal fields **W** and **B** have approximately complementary distributions in magnitude, which helps reduce the flowmeter error in measuring non axisymmetric flows. Mathematically, this means that the term $\mathbf{W}\times\mathbf{B}$ can be neglected from the integral equation [Eq. (3b)] if $\mathbf{W}\times\mathbf{B}=\text{const}\cdot\vec{z}$, where $\vec{z}$ is a unit vector in the z-direction (Fig. 3). The average flow velocity in the MV can thus be accurately measured.

B. Flow-rig experiments

Fully developed and distorted flow experiments are both carried out on a flow-rig setup (Fig. 1). To create different flow structures in the measuring pipe, a flange with baffles is installed at the inflow port of the EMF to distort the flow as illustrated in Figs. 14(a) and 14(b). When no baffle is installed, the flow will be fully developed in the measuring pipe.

In the fully developed flow experiment, the sensitivity of the EMF transducer is experimentally determined at several different flow rates. In the distorted flow experiments, the measuring error caused by the distorted flow structures is obtained with no change made in the flowmeter. The procedures of the two experiments (fully developed and distorted flow) are detailed as follows.

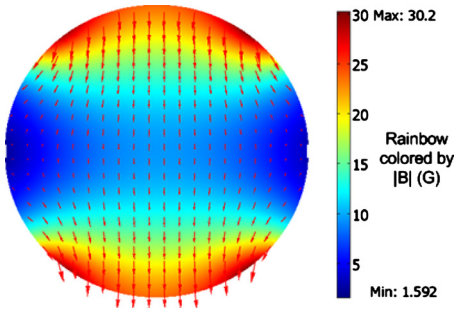

FIG. 13. (Color online) Sliced contour and vector arrows of **B** at $z=0$ mm.

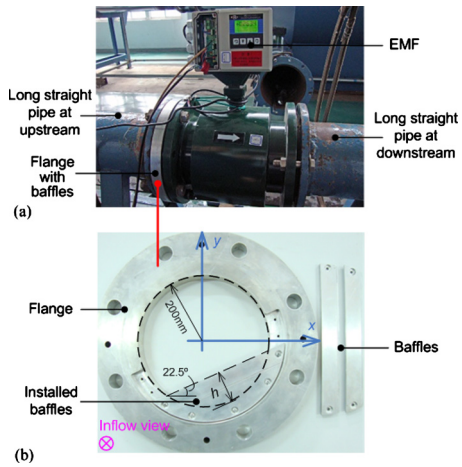

FIG. 14. (Color online) Illustration of flow-rig experiments: (a) installation of the EMF with baffles at inflow port; (b) illustration of the baffles.

1. Fully developed flow experiment

The EMF was calibrated for three flow velocities ($v_i=0.53$, 2.65, and 5.30 m/s) corresponding to Reynolds numbers of 10.61×10^5, 45.30×10^6, and 10.61×10^6) which are in the turbulent regime. Accordingly, the fully developed velocity profiles are expected to be relatively uniform. The measuring error δ defined in Eq. (7) is experimentally obtained

$$\delta=(Q_{\text{EMF}}-Q_{\text{tank}})/Q_{\text{tank}}, \tag{7}$$

where Q_{EMF} is the total water-volume measured by the EMF for a specified period of time; and Q_{tank} is the actual water-volume accumulated in the standard metal tanks.

To provide a basis for comparing the sensitivity of the dry calibrated EMF against that of the flow-rig test in terms of the error in Eq. (7), a hardware simulator (composing of a resistor divider network and amplifer[22]) is employed to generate a voltage signal ΔU_{EE}^S in phase but variable magnitude with ΔU_{EE}^S on the EMF electrodes. Using the hardware simulator to provide a display on the SPU (Fig. 2), the conversion factor of the SPU can be determined from $K_2=v/\Delta U_{EE}^S$ where v is the displayed velocity on the SPU screen. Equation (7) can be expressed as

$$1+\delta=\frac{Q_{\text{EMF}}}{Q_{\text{tank}}}=\frac{v(\Delta U_{EE})}{v_a(\Delta U_{EE}^S)}, \tag{8}$$

where v_a is the actual velocity. Thus, the sensitivity of the EMF at each tested flow rate can be calculated from Eq. (9)

$$S_{Ei}=\Delta U_{EE}/v_a=(\delta_i+1)/K_{2i}, \tag{9}$$

where denotes at the subscript "i" denotes the quantity computed for the ith tested flow rate.

2. Distorted flow experiment

In this experiment, a flange with specially designed baffles is installed at the inflow port of the EMF to distort the fluid flow field in the measuring pipe of the flowmeter as illustrated by Fig. 14(b), where the effective flow area is characterized by the parameter h defined in Fig. 14(c) indicating the height of the installed baffle. The baffles are in-

TABLE II. Baffle-settings and flow conditions.

Number of baffles	h (mm)	v_i (m/s)
1	25	0.54, 2.28, 4.66
2	50	0.48, 2.28, 4.60
3	75	0.41, 2.24, 4.59
4	100	0.44, 2.31, 4.55

stalled on the flange at an angle of 22.5° from the x-axis (Fig. 9). The baffle-settings and their corresponding flow conditions used in the tests are summarized in Table II. Small differences between the tested flow velocity points v_i are due to the flow control characteristics of the flow-rig setup at different pipe pressures (caused by the throttling roles of different baffle numbers).

C. Computation and verification of dry calibration

All the numerical computations were based on the actual sizes of the EMF, pipes and baffles [Fig. 14(b)] as illustrated in Fig. 6. Computations are performed on an IBM workstation (IBM System X3850M2, 4-way quad-core 2.4GHz CPU, 64 GB RAM).

1. Fully developed flow computation and verification

For fully developed flow, the velocity is assumed to have a uniform profile in the sensitivity computation; thus, the NS equations [Eq. (6)] for the flow velocity **v** are excluded from the computation. A total of 661 218 degrees of freedoms are computed on 74 664 triangular prism elements in about 30 min.

The results of **B** and **W** have been given previously in Figs. 12 and 13. The computed sensitivity is compared against that obtained from the flow-rig in Table III, where the max relative error of the dry calibration is defined relative to the flow-rig calibrated sensitivity S_D as

$$\text{Max relative error} = \text{Max}\left[\frac{S_D - S_{Ei}}{S_E} \times 100\%\right]. \qquad (10)$$

The small relative error of 0.271% validates the method of dry calibration for this kind of fully developed flow.

Special cares were made to reduce the errors, which lead to 0.2% error reduction by estimating the field in the MDD and additional 0.85% reduction in errors by using structured grids in the computation. The remaining 0.271% error could be due to the errors associated with the measured BCs and MVs. Especially the error associated with the measured magnetic BC, which has a maximum error of ±0.20% against actual field data, is found to be the largest contributor of the error in the dry-calibration method.

TABLE III. Comparison between flow-rig and dry calibrations.

Flow-rig calibrated sensitivity S_{Ei} [mV/(m/s)]			Dry calibrated sensitivity S_D [mV/(m/s)]	
0.53 m/s	2.65 m/s	5.30 m/s	Sensitivity	Max. error
0.111221	0.111049	0.110898	0.111199	0.271%

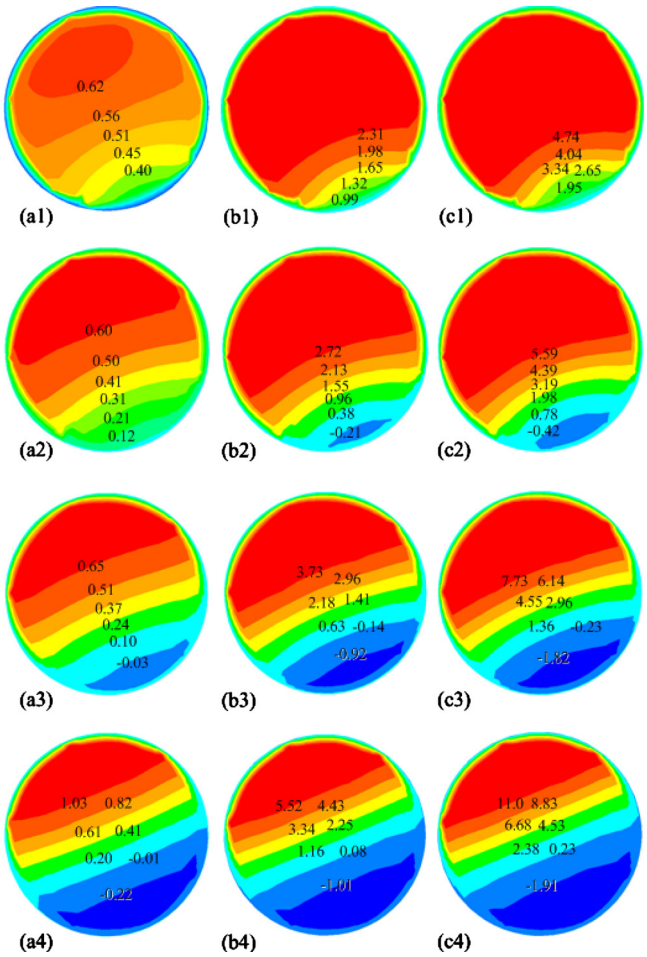

FIG. 15. (Color online) Axial flow velocity profiles (m/s) at electrodes-on section (z=0 mm), for different parameter sets (h,v) [units (mm, m/s)]: (al) (25, 0.54); (bl) (25, 2.28); (cl) (25,4.66); (a2) {50, 0.48); (b2) (50, 2.28); (c2) (50,4.60); (a3) (75, 0.41); (b3) (75, 2.24); (c3) (75,4.59); (a4){100, 0.44); (m) (100, 2.31); (c4) (100, 4.55).

2. Distorted flow computation and verification

The distorted flow on the velocity field **v** has been accounted for by the NS equations [Eq. (6)] along with a series of computation models built to characterize the different baffle height h. The axial flow velocity profiles at the electrode-on section (z=0 mm) for different parameter sets (h,v) are given by Fig. 15 showing that the velocity profiles are seriously distorted by the baffles. Vortexes are generated in the domains near the baffles (in a range of about one diameter at downstream).

The computed measuring errors of the flowmeter caused by the distorted flows are compared against experimental data in Fig. 16, which excellently agree validating the multiphysical computation of the fields. The small deviations could be due to the flow field computation, a common engineering challenge to perfectly simulate the actual flow field by solving the NS equations.

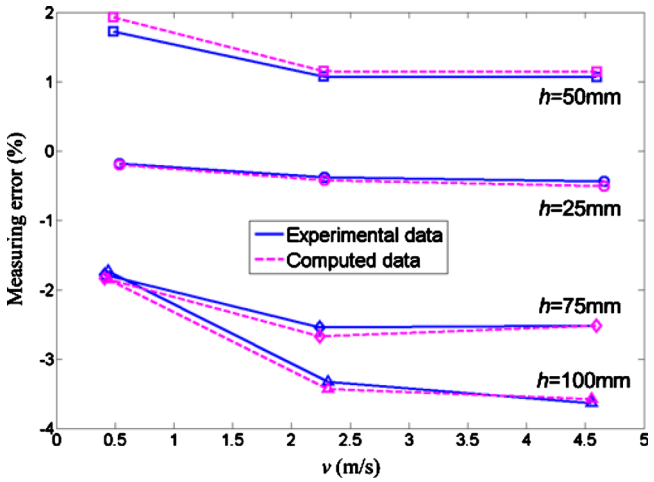

FIG. 16. (Color online) Comparison of the flowmeter measuring error obtained by dry calibration and flow-rig experiment.

VI. SUMMARY

A method for dry calibration of an EMF, which numerically solves the governing PDEs for the multiphysical fields (**B**, **W**, and **v**) with measured BCs, has been presented. This method offers highly precise calibration of medium and large EMFs (with diameters ranging from 200 mm to nearly indefinitely large values) without relying on any additional correction. This proposed dry-calibration method is time-efficient for solving calibration problems of large EMFs requiring only about 1 h (about equally divided between measurement and computation) to complete an EMF calibration.

The dry-calibration method has been experimentally verified by comparing computed sensitivities of a dry calibrated EMF against those obtained on a standard flow-rig setup. Based on a well orchestrated series of tests on a 200 mm-diameter EMF with fully development flow at different flow rates, the error relative to conventional flow-rig calibration was found to be smaller than 0.3%. An additional large number of tests on several EMFs from different manufactures confirm that errors in the range of $\pm 0.5\%$ can be consistently obtained. The robustness of the dry-calibration method has been experimentally investigated by means of distorting the inflow to the EMF being tested. Experiments validate that the method is robust against distorted flows for practical implementation.

Being an indirect method, the precision of the dry calibration, however, is still somewhat lower than the conventional (direct) flow-rig methods (with relative errors in the order of $\pm 0.05\%$ to $\pm 0.2\%$). Especially for some EMFs having very small measuring errors (0.2%, conventional EMFs 0.5%), the precision of the dry-calibration method needs further improvements. This paper offers methods to improve

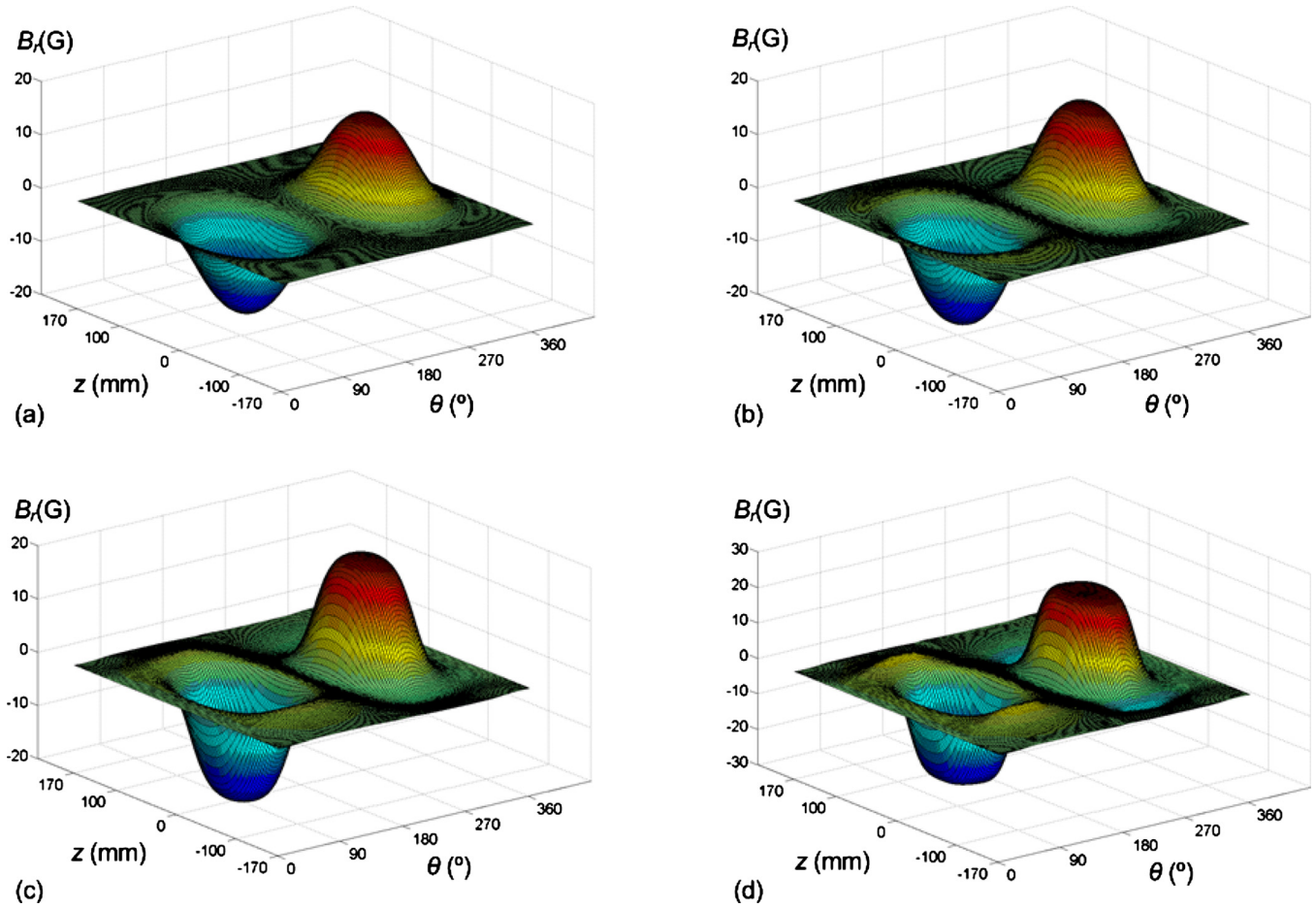

FIG. 17. (Color online) Reconstructed B_r used to estimate the BC on actual pipe surface ($r=100.137$ mm): (a) B_r at $r=60$ mm; (b) B_r at $r=70$ mm; (c) B_r at $r=80$ mm; (d) B_r at $r=90$ mm.

TABLE IV. Measurement of measuring pipe diameter.

z (mm)	θ (rad)							
	0	$\pi/8$	$\pi/4$	$3\pi/8$	$\pi/2$	$5\pi/8$	$3\pi/4$	$7\pi/8$
80	201.74	201.87	201.03	199.64	198.07	198.53	200.01	200.59
60	201.64	201.71	201.21	199.62	198.04	198.21	199.68	200.73
40	201.92	201.58	201.04	199.58	198.04	198.00	199.52	200.96
20	201.58	201.71	200.97	199.51	197.67	198.30	199.40	200.95
0	···	201.79	201.27	199.52	···	198.80	199.36	200.92
−20	201.58	201.74	201.42	199.57	197.76	198.84	199.46	200.73
−40	201.90	201.87	201.61	199.65	198.00	199.57	199.91	201.00
−60	201.97	201.88	201.65	199.93	198.46	199.68	200.10	200.99
−80	201.89	201.69	201.57	200.11	198.78	199.97	200.12	201.08

dry calibration by introducing field estimation in the MDD and structured grids, which lead to a reduction in errors by 0.2% and 0.85%, respectively. Further work should focus on reducing errors in the measured BCs.

As illustrated in this paper, the method for determining a physical field (such as magnetic, electric, and thermal) by solving the governing PDE with measured BCs is not only effective but a general approach. Additionally, the BC measurement can be automated to enhance the efficiency of dry calibration without sacrificing precision.

ACKNOWLEDGMENTS

The authors are grateful to the financial support of the National Natural Science Foundation of China (Grant No. 91023015), Zhejiang Provincial Natural Science Foundation of China (Grant Nos. R105008 and 1080038), and International S&T Cooperation Program of China (Grant No. 2008DFR70410).

APPENDIX

Measured diameters (position and values) are given in Table IV.

[1]J. A. Shercliff, *The Theory of Electromagnetic Flow-Measurement* (Cambridge University Press, London, 1962).
[2]ISO9104:1991, Measurement of fluid flow in closed conduits–Methods of evaluating the performance of electromagnetic flow-meters for liquids, International Organization for Standardization, 1991.
[3]J. Hemp, Flow Meas. Instrum. **12**, 123 (2001).
[4]M. K. Bevir, IEEE Trans. Magn. **6**, 315 (1970).
[5]M. K. Bevir, V. T. O'Sullivan, and D. G. Wyatt, J. Phys. D **14**, 373 (1981).
[6]D. G. Wyatt, J. Phys. D **16**, 465 (1983).
[7]V. T. O'Sullivan and D. G. Wyatt, J. Phys. D **16**, 1461 (1983).
[8]R. H. Al-Rabeth and R. C. Baker, J. Phys. E **19**, 203 (1986).
[9]J. Hemp and H. K. Versteeg, J. Phys. D: Appl. Phys. **19**, 1459 (1986).
[10]I. D. Vel't and Yu. V. Mikhailova, Meas. Tech. **48**, 249 (2005).
[11]I. D. Vel't and Yu. V. Mikhailova, Meas. Tech. **49**, 472 (2006).
[12]X. Fu, L. Hu, H. B. Xie, and H. Y. Yang, Chin. J. Mech. Eng. **43**, 26 (2007).
[13]J. Hemp, J. Phys. D: Appl. Phys. **24**, 244 (1991).
[14]Y. B. Li, Z. Q. Lin, S. Jack Hu, and G. L. Chen J. Appl. Phys. **101**, 053506 (2007).
[15]C. Kumar and L. H. Friedman, J. Appl. Phys. **101**, 094903 (2007).
[16]M. L. David, F. Pailloux, D. Babonneau, M. Drouet, J. F. Barbot, E. Simoen, and C. Claeys, J. Appl. Phys. **102**, 096101 (2007).
[17]C. C. Smyth, J. Phys. E **4**, 29 (1971).
[18]C. Hu, K.-M. Lee, and X. Fu, IEEE/ASME Trans. Mechatron. **15**, 728 (2010).
[19]G. K. Batchelor, *An Introduction to Fluid Dynamics*, 2nd ed. (Cambridge University Press, UK, 2002).
[20]A. E. Fitzgerald, C. Kingsley, Jr. and S. D. Umans, *Electric Machinery*, 6th ed. (Tsinghua University Press, China, 2003).
[21]J. H. Mathews and K. K. Fink, *Numerical Methods Using Matlab*, 4th ed. (Prentice-Hall, Englewood Cliffs, NJ, 2004).
[22]W. C. Cai, Z. Y. Ma, G. F. Qu, and S. L. Wang, *Electromagnetic Flowmeters* (Petrochemical Press, Beijing, 2004).